Supplemental Material for "Self-organized epigenetic signal processing in active chromatin"

Xu-Ze Zhang,[1] Hai-Zhen Long,[2] Hao-Yue Zhang,[2] and Kai Huang[1,*]

[1] *Institute of Systems and Physical Biology, Shenzhen Bay Laboratory, Shenzhen 518132, China.*
[2] *Institute of Molecular Physiology, Shenzhen Bay Laboratory, Shenzhen 518132, China.*

(Dated: September 10, 2026)

I. MICROSCOPIC MODEL AND SIMULATION METHODS

A. Chromatin and trans-factor representation

We model chromatin as a flexible bead–spring polymer containing N beads. Each bead carries a binary internal state, U or M. The state M represents a generic active histone modification, with H3K27ac as a representative example.

The polymer is surrounded by N_W mobile single-bead particles denoted by W. These particles represent writing-related trans-factors, including writing enzymes, mark-binding proteins, and multivalent coactivators. They describe a collective regulatory function rather than a single molecular species. A representative snapshot is shown in Fig. S1.

The reference polymer contains $N = 2000$ beads and represents a chromatin segment of approximately 1Mbp. A central interval is designated as the focal region Ω. Its size is varied from $N_\Omega = 10$ to 100 beads, corresponding to approximately 5–50kbp. The reference value used in most simulations $N_\Omega = 50$ corresponds to approximately 25kbp. Using a mammalian nucleosome repeat length of approximately 200 bp, this range can accommodate roughly 25–250 nucleosomes [1]. This scale is larger than the core sequence of a conventional enhancer and instead represents its surrounding modified chromatin. Conventional enhancers are typically sub-kilobase, whereas extended enhancer domains, often described as stretch enhancers or super-enhancers, can span several to tens of kilobases [2, 3]. We therefore interpret Ω as a localized active regulatory domain, which may contain an enhancer or promoter together with its surrounding chromatin, or an extended enhancer cluster. The effective chromatin-bead diameter is set to

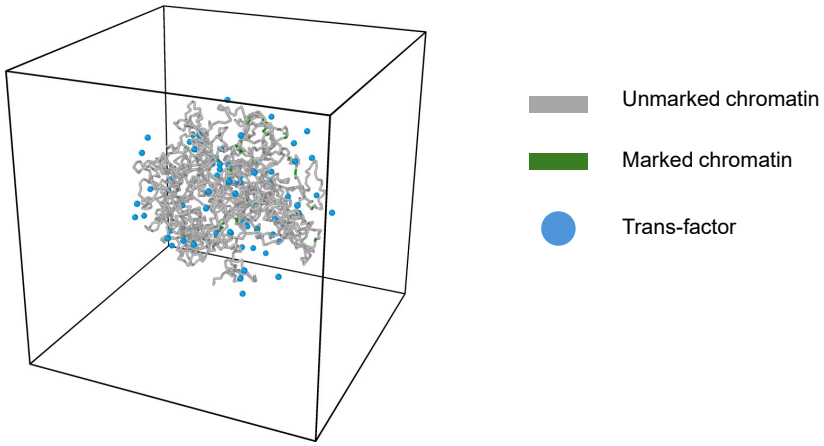

FIG. S1. Microscopic chromatin–factor model. Representative simulation snapshot of the chromatin polymer and mobile trans-factors. Unmarked (U) and marked (M) chromatin beads are shown in gray and green, respectively, and trans-factors (W) are shown in blue.

* huangkai@szbl.ac.cn

$\sigma = 20$nm. This mapping is approximate because the spatial organization of a chromatin segment depends on its genomic context and compaction state [4, 5].

B. Intra- and inter-molecular interactions

Adjacent chromatin beads are connected by a harmonic bond,

$$U_{\mathrm{bond}}(r) = \frac{k_{\mathrm{b}}}{2}(r - r_0)^2, \tag{S1}$$

where k_{b} is the bond stiffness and r_0 is the equilibrium bond length. We set $k_{\mathrm{b}} = 50\, k_{\mathrm{B}}T/\sigma^2$ and $r_0 = 1.0\sigma$.

All nonbonded interactions are described by a truncated Lennard–Jones potential,

$$U_{\mathrm{LJ}}^{ab}(r) = \begin{cases} 4\epsilon_{ab}\left[\left(\dfrac{\sigma_{ab}}{r}\right)^{12} - \left(\dfrac{\sigma_{ab}}{r}\right)^{6}\right], & r \le r_{\mathrm{c}}, \\ 0, & r > r_{\mathrm{c}}, \end{cases} \tag{S2}$$

where $a, b \in \{U, M, W\}$. Here, ϵ_{ab} is the interaction strength and σ_{ab} is the pair contact diameter. Chromatin beads have diameter $\sigma_U = \sigma_M = \sigma$, whereas the trans-factors have diameter $\sigma_W = 0.5\sigma$. The pair diameters follow the arithmetic mixing rule,

$$\sigma_{ab} = \frac{\sigma_a + \sigma_b}{2}. \tag{S3}$$

Thus,

$$\sigma_{UU} = \sigma_{UM} = \sigma_{MM} = \sigma, \qquad \sigma_{UW} = \sigma_{MW} = 0.75\sigma, \qquad \sigma_{WW} = 0.5\sigma. \tag{S4}$$

The cutoff is $r_{\mathrm{c}} = 2.5\sigma$ for all pairs.

The reference interaction strengths are

$$\epsilon_{MW} = 2.5\, k_{\mathrm{B}}T, \qquad \epsilon_{WW} = 1.0\, k_{\mathrm{B}}T, \qquad \epsilon_{\mathrm{other}} = 0.2\, k_{\mathrm{B}}T. \tag{S5}$$

Marked chromatin therefore has a strong affinity for W factors. The factors have a weaker self-attraction. All remaining interactions retain the same weak background value. In particular, no additional mark-dependent attraction is assigned between marked chromatin beads.

The strong M–W interaction represents reader-like recognition of active histone marks by writing-related factors [6–10]. The weaker W–W interaction represents weak multivalent association among active-chromatin regulators [11–13]. The polymer and trans-factors are confined within a spherical cavity of radius $R = 18.61\sigma$. The corresponding confinement volume is $V = 4\pi R^3/3$.

C. Epigenetic-state reactions

Each chromatin bead undergoes stochastic transitions between the unmarked and marked states,

$$U_i \underset{k_-}{\overset{k_i^+}{\rightleftharpoons}} M_i. \tag{S6}$$

The mark-loss rate k_- is spatially uniform. It represents enzymatic erasure, histone replacement, and other unresolved processes that remove the mark [14, 15].

The writing rate depends linearly on the instantaneous abundance of nearby W factors,

$$k_i^+ = w_i q_W(\mathbf{R}_i), \tag{S7}$$

where w_i is the local writing propensity. The local factor abundance is evaluated as

$$q_W(\mathbf{R}_i) = \sum_{j \in W} K(r_{ij}), \tag{S8}$$

with the reaction kernel

$$K(r) = \left(1 - \frac{r}{r_{\mathrm{K}}}\right) \Theta(r_{\mathrm{K}} - r). \tag{S9}$$

Here, r_{ij} is the distance between chromatin bead i and factor j, and $r_{\mathrm{K}} = 1.5\sigma$ is the reaction range. Factors closer to the chromatin bead contribute more strongly to its writing rate.

The effective volume sampled by the reaction kernel is

$$V_{\mathrm{K}} \equiv \int_{\mathbb{R}^3} K(r)\, d\mathbf{r} = \frac{\pi r_{\mathrm{K}}^3}{3}. \tag{S10}$$

For a spatially uniform factor distribution with density $\rho_W = N_W/V$, the expected local abundance is $\rho_W V_{\mathrm{K}}$. It should be noted that Eq. (S7) describes the unsaturated limit in which writing is proportional to local factor abundance [16].

The writing propensity is enhanced within the focal region,

$$w_i = \begin{cases} \chi_\Omega w_0, & i \in \Omega, \\ w_0, & i \notin \Omega, \end{cases} \tag{S11}$$

where w_0 is the background propensity and χ_Ω is the relative enhancement within Ω. The focal interval represents a chromatin region selected by sequence-specific regulatory activity, such as transcription-factor binding at an enhancer or promoter [17].

Within Ω, the quantities entering the dimensionless regulatory input are related by

$$a = \frac{\chi_\Omega w_0 \rho_W V_{\mathrm{K}}}{k_-}. \tag{S12}$$

The local writing enhancement χ_Ω and the global factor density ρ_W can therefore be varied independently while producing the same regulatory input a.

D. Hybrid molecular-dynamics and reaction scheme

The chromatin polymer and trans-factors are evolved by Langevin molecular dynamics using HOOMD-blue [18]. The bead diameter σ, thermal energy $k_{\mathrm{B}}T$, and particle mass define the reduced units. The integration time step is

$$\Delta t_{\mathrm{MD}} = 0.005\, \tau_{\mathrm{MD}}. \tag{S13}$$

The internal chromatin states are updated every 100 molecular dynamics steps. The reaction-update interval is therefore

$$\Delta t_{\mathrm{update}} = 0.5\, \tau_{\mathrm{MD}}. \tag{S14}$$

For each bead, the probability of the allowed state transition during this interval is calculated by

$$P = 1 - \exp\left(-\lambda \Delta t_{\mathrm{update}}\right), \tag{S15}$$

where $\lambda = k_i^+$ for an unmarked bead and $\lambda = k_-$ for a marked bead. The writing rate is evaluated from the simulated snapshot at each reaction update. A state transition immediately changes the nonbonded interactions of that chromatin bead.

Simulation time is reported using dimensionless time

$$\tau = k_- t. \tag{S16}$$

The background writing propensity and loss rate are fixed in all simulations at $w_0 = 3.0 \times 10^{-4}\, \tau_{\mathrm{MD}}^{-1}$ and $k_- = 2.0 \times 10^{-4}\, \tau_{\mathrm{MD}}^{-1}$, respectively. Unless otherwise stated, all other parameters are held fixed. The regulatory input is changed through χ_Ω and ρ_W.

Initial polymer conformations are generated by a self-avoiding random walk within the spherical cavity. The W factors are then inserted at random positions without overlap with the polymer beads or other factors. Static-state simulations are initialized from either a fully unmarked state, $\hat{m}(0) = 0$, or a fully marked state, $\hat{m}(0) = 1$. At least 20 independent trajectories were generated for each parameter set. Most trajectories are evolved for up to $2.0 \times 10^7\, \Delta t_{\mathrm{MD}}$, corresponding to a maximum reduced time of $\tau = 20$. Further simulation details about one-step perturbation, activation-maintenance, and periodic input are described in the corresponding sections.

II. MEASUREMENT AND VALIDATION OF THE CONDITIONAL ENRICHMENT

A. Measurement of $\mathcal{G}$ from simulation trajectories

We measured $\mathcal{G}$ from the simulated configurations using the reaction kernel in Eq. (S9). Let $x_i^{(k)}(s) = 1$ if bead i is marked in frame s of trajectory k, and $x_i^{(k)}(s) = 0$ otherwise. The mark fraction in this frame is

$$\hat{m}_k(s) = \frac{1}{N_\Omega} \sum_{i\in\Omega} x_i^{(k)}(s). \tag{S17}$$

The conditional enrichment $\mathcal{G}(u)$ is the factor abundance sampled by an unmarked bead, normalized by the uniform expectation $\rho_W V_{\mathrm{K}}$. Here, u labels a sampled value of the instantaneous mark fraction. For trajectory k, it is estimated as

$$\begin{aligned}\mathcal{G}_k(u) &= \frac{1}{N_k^{\mathrm{fr}}(u)} \sum_{s:\hat{m}_k(s)=u} \frac{\sum_{i\in\Omega} \left[1 - x_i^{(k)}(s)\right] q_i^{(k)}(s)}{N_\Omega(1-u)\rho_W V_{\mathrm{K}}} \\ &= \frac{V}{V_{\mathrm{K}}} \frac{1}{N_k^{\mathrm{fr}}(u)} \sum_{s:\hat{m}_k(s)=u} \frac{\sum_{i\in\Omega} \left[1 - x_i^{(k)}(s)\right] q_i^{(k)}(s)}{N_W N_\Omega(1-u)},\end{aligned} \tag{S18}$$

where $q_i^{(k)}(s)$ is the kernel-weighted local factor abundance defined by Eq. (S8), and $N_k^{\mathrm{fr}}(u)$ is the number of frames in trajectory k with mark fraction u. The second equality follows from $\rho_W = N_W/V$. The normalization ensures that $\mathcal{G}(u) = 1$ for a spatially uniform factor distribution.

Each trajectory provides one conditional estimate at every sampled value of u. For an ensemble of independent trajectories, these estimates are averaged with equal weight,

$$\mathcal{G}(u) = \frac{1}{N_{\mathrm{traj}}(u)} \sum_{k=1}^{N_{\mathrm{traj}}(u)} \mathcal{G}_k(u), \tag{S19}$$

where $N_{\mathrm{traj}}(u)$ includes only trajectories that visit u.

B. Dependence of $\mathcal{G}$ on regulatory conditions and history

The reduction of the microscopic dynamics assumes that the conditional enrichment can be closed by the instantaneous mark fraction,

$$\mathcal{G} = \mathcal{G}(u). \tag{S20}$$

This closure is not guaranteed. At the same $\hat{m} = u$, the chromatin–factor organization may still depend on the regulatory input or on the path by which the state was reached. A strong residual dependence would require additional variables beyond mark fraction.

We test this closure at three levels. We first compare $\mathcal{G}(u)$ over a broad range of regulatory inputs a. We then compare trajectories initialized from the fully unmarked and fully marked states. This tests whether configurations with the same mark fraction retain a dependence on their initial state.

Finally, we resolve the regulatory input into its two independently controlled components, ρ_W and χ_Ω. Although ρ_W and χ_Ω enter a multiplicatively, they have different microscopic roles. The factor density ρ_W changes the global factor abundance and may alter the spatial organization. In contrast, χ_Ω changes the writing propensity within Ω without directly changing the molecular interactions. We therefore examine $\mathcal{G}(u)$ throughout the (ρ_W, χ_Ω) parameter space. All conditional averages are obtained independently before comparison. These tests determine whether the spatial feedback can be represented by a single function of the instantaneous mark fraction.

Figs. S2 and S3 summarize these tests. For each parameter condition, a value of $\mathcal{G}(u)$ was retained only when the corresponding u was visited by at least eight independent trajectories. This criterion leaves gaps in the intermediate transition region for many conditions. Once the positive feedback is activated, the system passes through this region

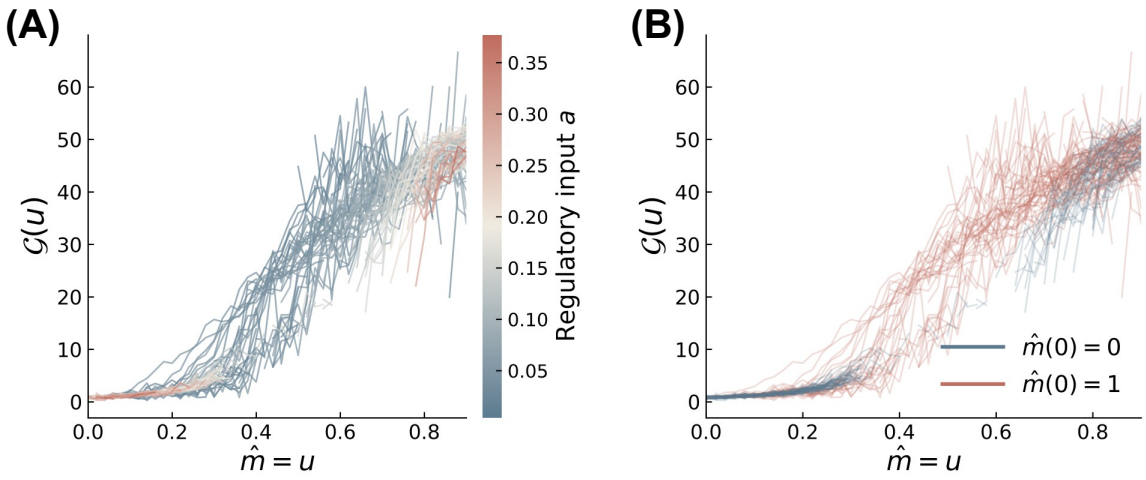

FIG. S2. (A) Conditional enrichment $\mathcal{G}(u)$ measured across the explored regulatory inputs. Each curve denotes a conditional average obtained separately for one parameter condition and is colored by its regulatory input a. (B) The same measurements grouped by the initial mark state, $\hat{m}(0) = 0$ (blue) and $\hat{m}(0) = 1$ (red). Values at a given u were retained only when that state was sampled by at least eight independent trajectories.

rapidly. Stronger regulatory inputs further accelerate this transition and make intermediate values difficult to sample. Nevertheless, the retained $\mathcal{G}(u)$ curves show an approximate collapse within a common range. No systematic dependence is observed on the input strength, the initial state, or whether a is varied through ρ_W or χ_Ω. These results support treating the conditional enrichment as a function of the instantaneous mark fraction alone within the explored parameter range.

C. Parameter-balanced consensus and Hill representation of $\mathcal{G}(m)$

The parameter-balanced consensus shown in Fig. 2B of the main text was constructed from all (ρ_W, χ_Ω) conditions. At each u, a parameter condition was retained only when at least eight independent trajectories visited that state. A consensus value was calculated only when at least twelve parameter conditions remained. Each valid condition was assigned equal weight. We restricted the analysis to $0 \le u \le 0.90$, because fewer unmarked beads remain at larger u. A Huber location estimator with tuning constant $c = 1.345$ was used to determine the robust center across parameter conditions [19]. The 16th–84th percentile range was used to describe the corresponding between-condition variation.

The pointwise robust centers were projected onto a non-decreasing curve using weighted isotonic regression. The weights were proportional to $\sqrt{n_{\mathrm{p}}(u)}/s(u)$, where $n_{\mathrm{p}}(u)$ is the number of contributing parameter conditions and $s(u)$ is their robust dispersion. The resulting points were connected by shape-preserving cubic interpolation. For use in the theoretical analysis, we represent the interpolated consensus as a continuous constitutive function of the mean-field state m. It was fitted by

$$\mathcal{G}(m) = \mathcal{G}_{\min} + A\frac{m^h}{K^h + m^h}, \tag{S21}$$

The same procedure was applied separately to the datasets with different interactions and N_Ω.

D. Radius of gyration of the active chromatin region

To characterize the conformational change of the focal chromatin region during the feedback process, we calculated its radius of gyration. For frame s of trajectory k,

$$R_{g,k}(s) = \left[\frac{1}{N_\Omega}\sum_{i\in\Omega}\left|\mathbf{R}_i^{(k)}(s) - \mathbf{R}_{\mathrm{cm}}^{(k)}(s)\right|^2\right]^{1/2}, \tag{S22}$$

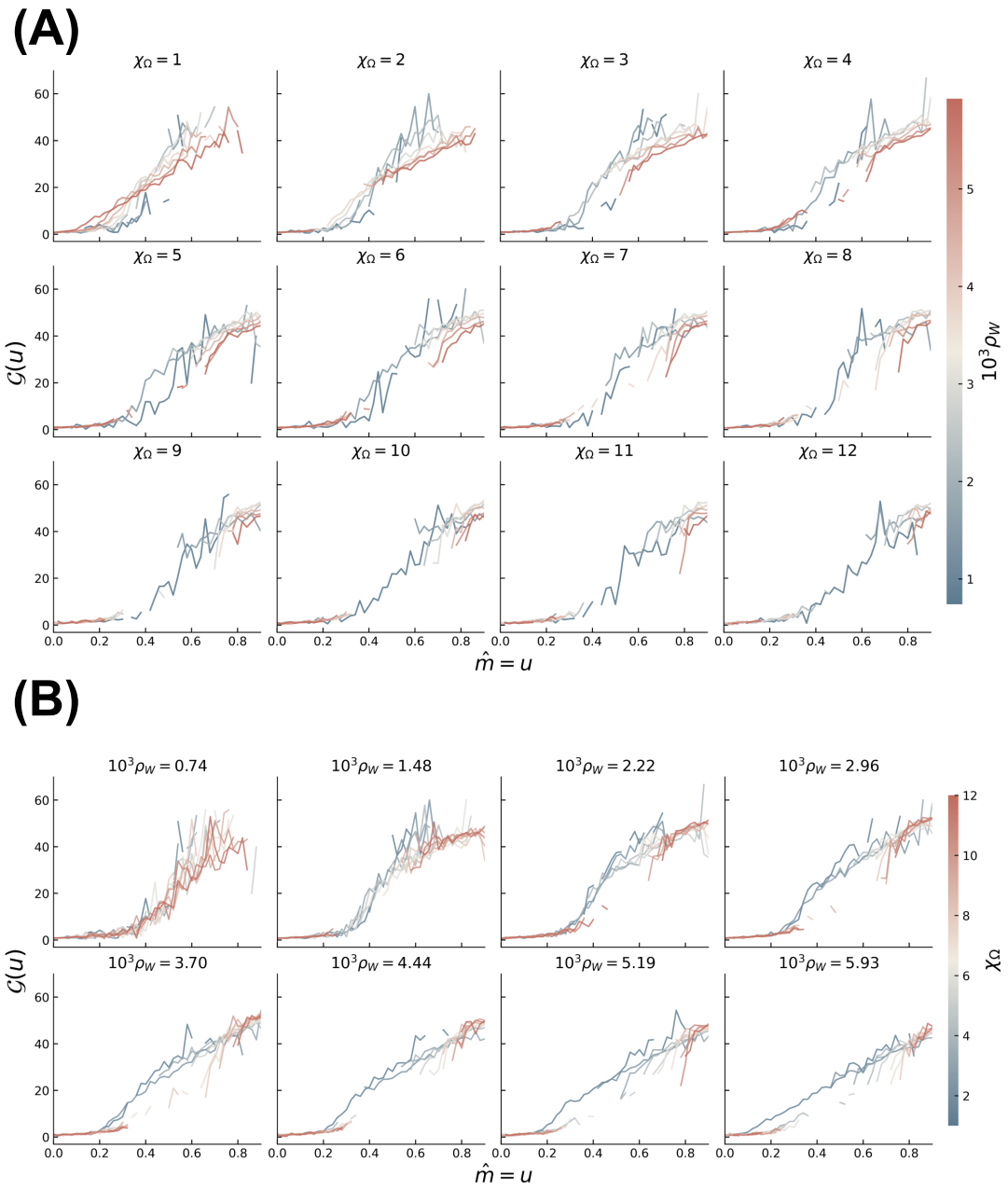

FIG. S3. (A) Conditional enrichment $\mathcal{G}(u)$ at fixed local writing enhancement χ_Ω, as indicated above each panel, while varying the factor density ρ_W; curves are colored by $10^3\rho_W$. (B) Conditional enrichment at fixed ρ_W, as indicated above each panel, while varying χ_Ω; curves are colored by χ_Ω.

where

$$\mathbf{R}_{\mathrm{cm}}^{(k)}(s) = \frac{1}{N_\Omega} \sum_{i \in \Omega} \mathbf{R}_i^{(k)}(s) \tag{S23}$$

is the center of mass of the chromatin beads within Ω.

The conditional radius of gyration $R_g(u)$ was calculated from the same trajectory ensemble used for $\mathcal{G}(u)$. For each (N_W, χ_Ω) condition, simulated frames were grouped according to their instantaneous mark fraction $\hat{m} = u$, and the corresponding R_g values were averaged over the sampled trajectories to obtain a conditional estimate. The results are shown in Fig. S4. The individual conditional values are shown as the raw data points. At each u, the reported

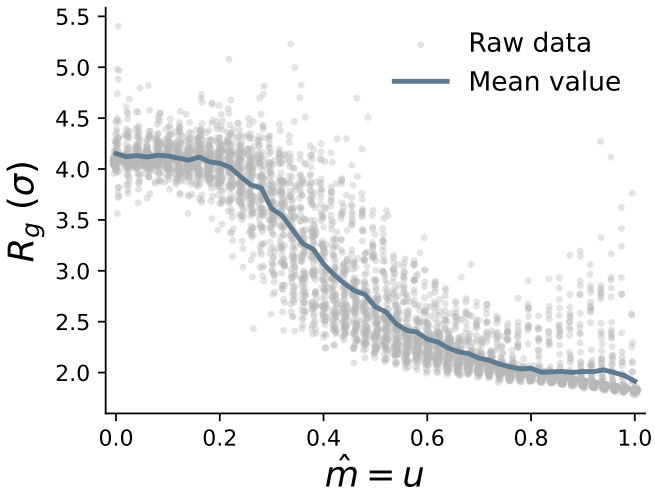

FIG. S4. Mean radius of gyration $R_g(u)$ as a function of the instantaneous mark fraction $\hat{m} = u$. Gray points show the conditional estimates obtained separately for different (N_W, χ_Ω) conditions. The blue solid curve shows the mean obtained by assigning equal weight to all sampled conditions at each u.

mean was then obtained by assigning equal weight to all sampled (N_W, χ_Ω) conditions.

E. Dependence of $\mathcal{G}$ on molecular interactions and region size

Although $\mathcal{G}$ depends only weakly on regulatory conditions and history, it remains sensitive to the intrinsic properties of the chromatin–factor system. We therefore examined how $\mathcal{G}$ changes with the mark–factor interaction ϵ_{MW}, the factor–factor interaction ϵ_{WW}, and the size of the region N_Ω.

To reduce the computational cost, all simulations in this subsection were performed at fixed $\chi_\Omega = 10$, while ρ_W was varied. For each parameter set, simulations were initialized separately from $\hat{m}(0) = 0$ and $\hat{m}(0) = 1$. The range of ρ_W was adjusted for different interaction strengths and region sizes to obtain sufficient sampling of the high-mark state. A separate parameter-balanced consensus curve was constructed for each dataset using the procedure described above, with each ρ_W condition assigned equal weight. Because these reduced parameter scans sampled some values of m less frequently, the minimum sampling requirement was relaxed. A condition-specific value of $\mathcal{G}(u)$ was retained when the corresponding u was visited by at least three independent trajectories.

Changing the molecular interactions directly modifies $\mathcal{G}$. Reducing ϵ_{MW} weakens the recruitment of trans-factors by marked chromatin and therefore substantially lowers $\mathcal{G}$ (Fig. 2B of the main text). Reducing ϵ_{WW}, which suppresses self-association among trans-factors, also lowers $\mathcal{G}$, but the change is minor (Fig. S5A). More generally, ϵ_{MW} and ϵ_{WW} provide two coupled contributions to factor enrichment. In realistic systems, stronger mark–factor recognition may partially compensate for weaker factor–factor association, and vice versa.

The region size produces a nonmonotonic change in $\mathcal{G}$ (Fig. S5B). The enrichment is weak for $N_\Omega = 10$, reaches its largest value at $N_\Omega = 25$, and then progressively decreases as N_Ω increases. At fixed mark fraction, a very small region contains too few marked beads to support strong collective factor recruitment. Increasing the region size therefore promotes the formation of a factor-rich structure. For larger regions, however, the finite factor pool is distributed over more chromatin sites, reducing the average enrichment sampled by each unmarked bead. This behavior reflects a competition between cooperative hub formation at small sizes and factor-limited dilution at large sizes.

III. BIRTH–DEATH DYNAMICS

A. Finite-N_Ω birth–death process

The mean-field equation describes the deterministic evolution of a continuous mark fraction. A finite chromatin region instead contains a discrete number of marked sites. Let $n = 0, 1, \ldots, N_\Omega$ denote the number of marked sites

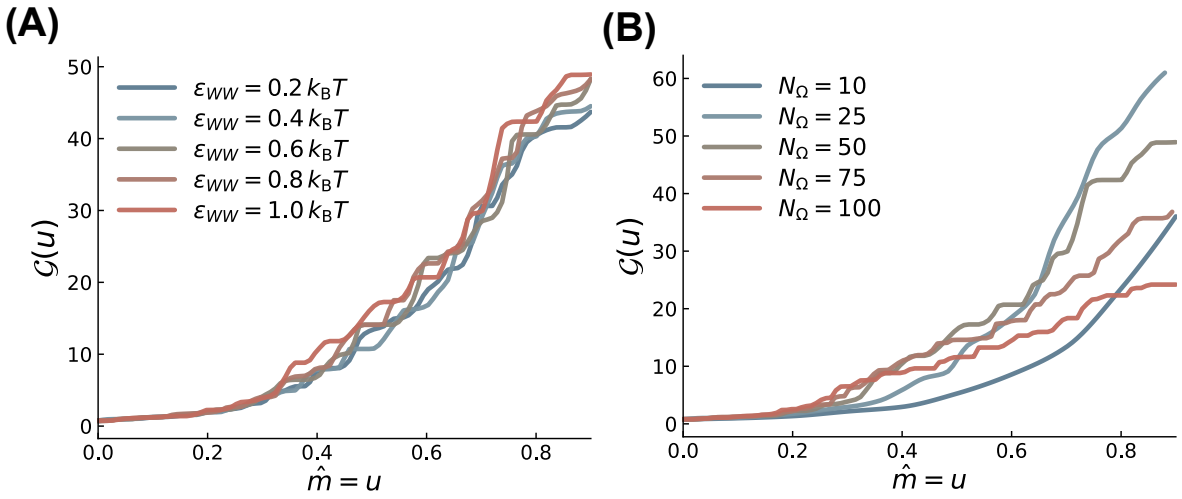

FIG. S5. (A) Parameter-balanced consensus curves $\mathcal{G}(u)$ for different factor–factor interaction strengths ϵ_{WW}. Reducing ϵ_{WW} weakly lowers the enrichment. (B) Consensus curves for different focal-region sizes N_Ω. The enrichment is weak for $N_\Omega = 10$, reaches its largest value at $N_\Omega = 25$, and decreases as the region is enlarged further. Each curve was constructed at fixed $\chi_\Omega = 10$ from the corresponding ρ_W scan.

and let

$$m_n = \frac{n}{N_\Omega} \tag{S24}$$

denote the mark fraction associated with state n. The mark number evolves through the one-step transitions

$$n \xrightarrow{\lambda_n} n+1, \qquad n \xrightarrow{\mu_n} n-1. \tag{S25}$$

At state n, the region contains $N_\Omega - n$ unmarked sites. Each unmarked site is written at the dimensionless rate $a\mathcal{G}(m_n)$. The total birth rate is therefore

$$\lambda_n = (N_\Omega - n) a \mathcal{G}\left(\frac{n}{N_\Omega}\right). \tag{S26}$$

Each marked site loses its mark at unit rate in the reduced time $\tau = k_- t$. The corresponding death rate is

$$\mu_n = n. \tag{S27}$$

The physical boundaries satisfy $\mu_0 = 0$ and $\lambda_{N_\Omega} = 0$.

Let $p_n(\tau)$ be the probability of observing n marked sites at time τ. Its evolution obeys

$$\frac{dp_n}{d\tau} = \lambda_{n-1} p_{n-1} + \mu_{n+1} p_{n+1} - (\lambda_n + \mu_n) p_n, \tag{S28}$$

where terms outside $0 \le n \le N_\Omega$ are omitted. Equations (S26)–(S28) define a classical one-step birth–death process [20–22]. Its state-dependent birth rate is supplied by the conditional enrichment $\mathcal{G}$ measured from the microscopic chromatin–factor dynamics.

The connection to the deterministic equation follows from the local moments of the process. Over a short interval $\Delta\tau$,

$$\begin{aligned} \mathbb{P}(\Delta n = 1 \mid n) &= \lambda_n \Delta\tau + \mathcal{O}(\Delta\tau^2), \\ \mathbb{P}(\Delta n = -1 \mid n) &= \mu_n \Delta\tau + \mathcal{O}(\Delta\tau^2). \end{aligned} \tag{S29}$$

The conditional mean increment of the instantaneous mark fraction is

$$\begin{aligned} \mathbb{E}\left[\Delta\hat{m} \mid n(\tau) = n\right] &= \frac{\lambda_n - \mu_n}{N_\Omega} \Delta\tau + \mathcal{O}(\Delta\tau^2) \\ &= \left[a(1 - m_n)\mathcal{G}(m_n) - m_n\right] \Delta\tau + \mathcal{O}(\Delta\tau^2). \end{aligned} \tag{S30}$$

The corresponding variance is

$$\begin{aligned}\mathrm{Var}\left[\Delta\hat{m} \mid n(\tau)=n\right] &= \frac{\lambda_n+\mu_n}{N_\Omega^2}\Delta\tau+\mathcal{O}(\Delta\tau^2)\\ &= \frac{a(1-m_n)\mathcal{G}(m_n)+m_n}{N_\Omega}\Delta\tau+\mathcal{O}(\Delta\tau^2).\end{aligned} \tag{S31}$$

In the limit $N_\Omega \to \infty$, the fluctuations vanish and Eq. (S30) recovers the deterministic equation in the main text. At fixed m and a, the amplitude of the finite-number fluctuations scales as $N_\Omega^{-1/2}$.

B. Finite-window first-passage statistics

First-passage statistics are calculated by treating the prescribed target region as absorbing. For the low-to-high process, define

$$n_{\mathrm{th}}^{L\to H} = \lceil N_\Omega m_{\mathrm{th}}^{L\to H} \rceil. \tag{S32}$$

The absorbing and transient state sets are

$$\begin{aligned}\mathcal{A}_{L\to H} &= n_{\mathrm{th}}^{L\to H},\ldots,N_\Omega,\\ \mathcal{T}_{L\to H} &= 0,\ldots,n_{\mathrm{th}}^{L\to H}-1.\end{aligned} \tag{S33}$$

For the high-to-low process, define

$$n_{\mathrm{th}}^{H\to L} = \lfloor N_\Omega m_{\mathrm{th}}^{H\to L} \rfloor, \tag{S34}$$

with

$$\begin{aligned}\mathcal{A}_{H\to L} &= 0,\ldots,n_{\mathrm{th}}^{H\to L},\\ \mathcal{T}_{H\to L} &= n_{\mathrm{th}}^{H\to L}+1,\ldots,N_\Omega.\end{aligned} \tag{S35}$$

The corresponding first-passage times are

$$\begin{aligned}T_{L\to H} &= \inf\{\tau>0 : n(\tau)\geq n_{\mathrm{th}}^{L\to H}\},\\ T_{H\to L} &= \inf\{\tau>0 : n(\tau)\leq n_{\mathrm{th}}^{H\to L}\}.\end{aligned} \tag{S36}$$

For $N_\Omega = 50$, the thresholds used in the main text give $n_{\mathrm{th}}^{L\to H}=25$ for $m_{\mathrm{th}}^{L\to H}=0.5$ and $n_{\mathrm{th}}^{H\to L}=10$ for $m_{\mathrm{th}}^{H\to L}=0.2$. The initial states are $n(0)=0$ and $n(0)=N_\Omega$, respectively.

For either direction $X\to Y$, let $\mathbf{p}(\tau)$ denote the probability vector restricted to the corresponding transient set $\mathcal{T}_{X\to Y}$. Its evolution is

$$\frac{d\mathbf{p}}{d\tau} = \mathbf{Q}_{X\to Y}\mathbf{p}, \tag{S37}$$

where the transient generator has matrix elements

$$(\mathbf{Q}_{X\to Y})_{ij} = \begin{cases}\lambda_j, & i=j+1,\\ \mu_j, & i=j-1,\\ -(\lambda_j+\mu_j), & i=j,\\ 0, & \text{otherwise,}\end{cases} \qquad i,j\in\mathcal{T}_{X\to Y}. \tag{S38}$$

A transition from the transient set into the absorbing set is omitted from the off-diagonal elements. Its rate remains in the corresponding diagonal element and therefore removes probability from the transient states.

For an initial probability vector $\mathbf{p}_0$, the transient-state distribution is

$$\mathbf{p}(\tau) = \exp\left(\mathbf{Q}_{X\to Y}\tau\right)\mathbf{p}_0. \tag{S39}$$

The survival probability is the probability that the threshold has not been crossed,

$$S_{X\to Y}(\tau) = \mathbf{1}^{\mathrm{T}}\mathbf{p}(\tau). \tag{S40}$$

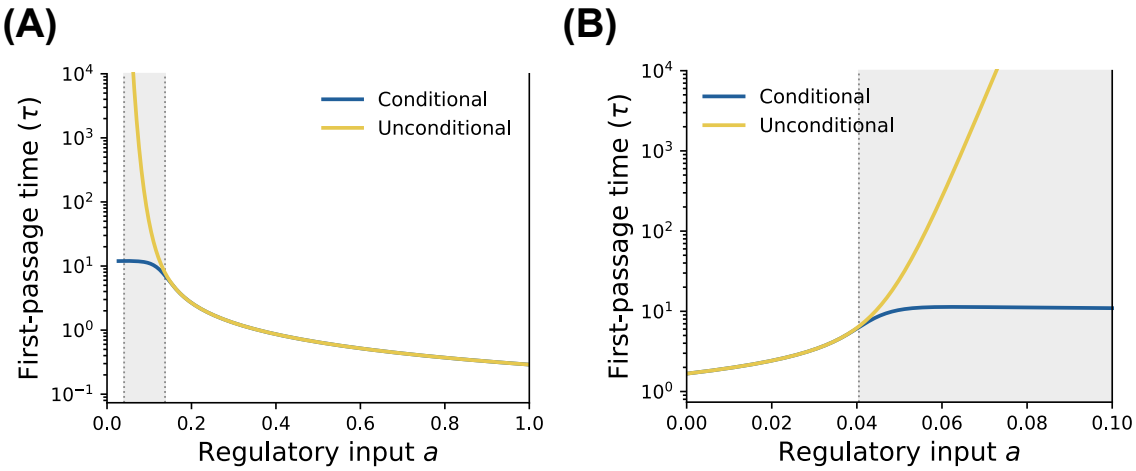

FIG. S6. (A) Low-to-high passage with $m_{\mathrm{th}}^{L\to H} = 0.5$. (B) High-to-low passage with $m_{\mathrm{th}}^{H\to L} = 0.2$. Results are calculated from the birth–death model at $N_\Omega = 50$. Blue curves show the mean conditioned on passage within $T_{\mathrm{obs}} = 20$, whereas yellow curves show the unconditional mean over an infinite time horizon. Gray shading denotes the deterministic MEMORY regime.

The theoretical finite-window passage probability is therefore

$$P_{X\to Y}(T_{\mathrm{obs}}) = 1 - S_{X\to Y}(T_{\mathrm{obs}}). \tag{S41}$$

The finite-trajectory expression used for the microscopic simulations is the sample estimator of Eq. (S41).

The first-passage-time density is

$$f_{X\to Y}(\tau) = -\frac{dS_{X\to Y}}{d\tau}. \tag{S42}$$

Only trajectories that cross the threshold within T_{obs} contribute to the simulated mean first-passage time. The corresponding theoretical quantity is

$$\langle T_{X\to Y}\rangle_{\mathrm{cond}} = \frac{\int_0^{T_{\mathrm{obs}}} \tau f_{X\to Y}(\tau)d\tau}{P_{X\to Y}(T_{\mathrm{obs}})}. \tag{S43}$$

Integration by parts gives

$$\langle T_{X\to Y}\rangle_{\mathrm{cond}} = \frac{\int_0^{T_{\mathrm{obs}}} S_{X\to Y}(\tau)d\tau - T_{\mathrm{obs}}S_{X\to Y}(T_{\mathrm{obs}})}{1 - S_{X\to Y}(T_{\mathrm{obs}})}. \tag{S44}$$

This quantity is bounded by T_{obs}. It remains finite when passage events are rare within the observation window.

For comparison, the unconditional mean first-passage time is

$$\langle T_{X\to Y}\rangle_{\infty} = \int_0^{\infty} \tau f_{X\to Y}(\tau)d\tau = \int_0^{\infty} S_{X\to Y}(\tau)d\tau = -\mathbf{1}^{\mathrm{T}}\mathbf{Q}_{X\to Y}^{-1}\mathbf{p}_0.$$

Unlike Eq. (S44), the unconditional mean can become extremely large when escape from the initial state is rare (Fig. S6).

The finite-window passage probability depends explicitly on T_{obs}. A longer observation window allows more trajectories to cross the prescribed threshold and therefore shifts the apparent transition boundary. This boundary is distinct from the saddle-node thresholds of the deterministic equation, which are independent of the observation time.

To test this dependence, the microscopic trajectories were truncated at different observation times. For each T_{obs}, the corresponding theoretical probability was calculated from Eq. (S41) without changing $\mathcal{G}(m)$ or any other model parameter. We define the probability residual as

$$\Delta P_{X\to Y}(T_{\mathrm{obs}}) = P_{X\to Y}^{\mathrm{sim}}(T_{\mathrm{obs}}) - P_{X\to Y}^{\mathrm{theory}}(T_{\mathrm{obs}}). \tag{S45}$$

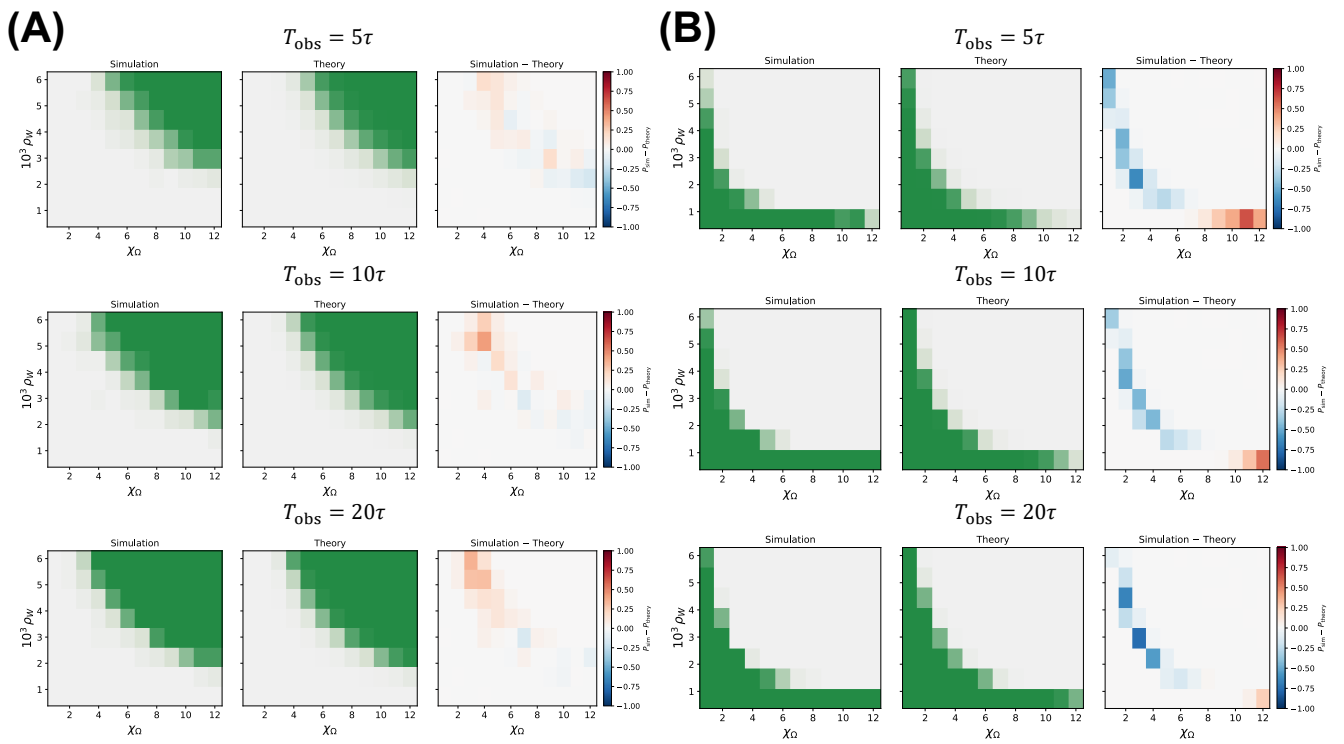

FIG. S7. (A) Low-to-high passage from $\hat{m}(0) = 0$ with $m_{\rm th}^{L\to H} = 0.5$. (B) High-to-low passage from $\hat{m}(0) = 1$ with $m_{\rm th}^{H\to L} = 0.2$. Rows correspond to observation windows $T_{\rm obs} = 5\tau$, 10τ, and 20τ. Within each row, the panels show from left to right, the simulated passage probability, the birth–death theory prediction, and the residual $\Delta P = P_{\rm sim} - P_{\rm theory}$ over the (χ_Ω, ρ_W) parameter space. Passage probabilities increase from white to green; positive and negative residuals are shown in red and blue, respectively.

Fig. S7 compares the simulated probabilities, the theoretical predictions, and their residuals at different observation times. Increasing $T_{\rm obs}$ shifts the passage boundaries in both directions. The birth–death theory systematically captures this displacement, with modest deviations near the transition region.

C. Stationary distribution and kinetic barriers

For a fixed regulatory input a, let $\pi_n(a)$ denote the stationary probability of observing n marked sites. The stationary distribution of the finite one-step process is

$$\pi_n(a) = \frac{w_n(a)}{\sum_{k=0}^{N_\Omega} w_k(a)}, \qquad w_0(a) = 1, \qquad w_n(a) = \prod_{j=0}^{n-1} \frac{\lambda_j(a)}{\mu_{j+1}}. \tag{S46}$$

The corresponding kinetic landscape is

$$\Delta\Phi(m_n; a) = -\ln\left[\frac{\pi_n(a)}{\max_{0\le k\le N_\Omega} \pi_k(a)}\right]. \tag{S47}$$

Thus, $\Delta\Phi = 0$ at the most probable mark fraction for each a. Within the bimodal range, let $n_{\rm L}$ and $n_{\rm H}$ denote the low- and high-mark local maxima of π_n, respectively. Let $n_{\rm U}$ denote the intervening local minimum, with

$$n_{\rm L} < n_{\rm U} < n_{\rm H}. \tag{S48}$$

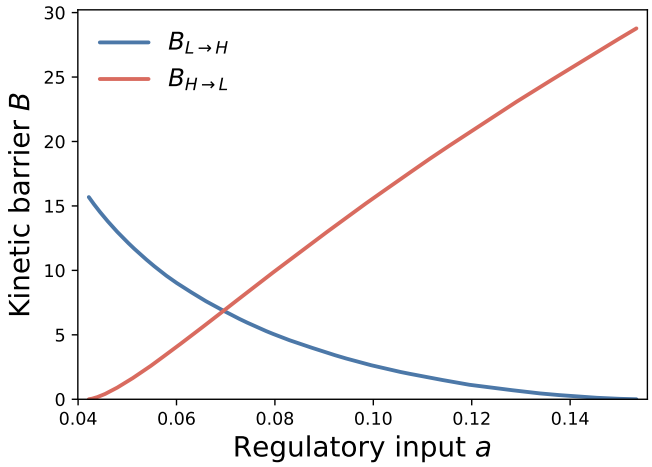

FIG. S8. The low-to-high barrier $B_{L\to H}$ (blue) and high-to-low barrier $B_{H\to L}$ (red) are calculated from the stationary kinetic landscape of the birth–death process at $N_\Omega = 50$.

Equivalently, n_{L} and n_{H} are the two local minima of the kinetic landscape, while n_{U} is the barrier between them. The directional barriers are defined as

$$\begin{aligned} B_{L\to H}(a) &= \Delta\Phi(m_{n_{\mathrm{U}}}; a) - \Delta\Phi(m_{n_{\mathrm{L}}}; a), \\ B_{H\to L}(a) &= \Delta\Phi(m_{n_{\mathrm{U}}}; a) - \Delta\Phi(m_{n_{\mathrm{H}}}; a). \end{aligned} \tag{S49}$$

As shown in Fig. S8, these quantities measure the stationary suppression of escape from the low- and high-mark basins, respectively.

IV. PERTURBATION AND RECOVERY ANALYSIS

Perturbation simulations were initialized from the fully marked state, $\hat{m}(0) = 1$. The system was first evolved for $\tau = 1$ with the epigenetic-state reactions active. A fraction f_{del} of the marks present within Ω was then deleted by changing the corresponding beads from M to U.

Both writing and loss reactions were suspended for the following $\tau = 1$, while the polymer and W factors continued to evolve by Langevin dynamics. The reactions were then restored, and the system was evolved for an additional $\tau = 10$. All interaction and regulatory parameters were unchanged throughout the simulation. Twenty independent trajectories were simulated for each parameter set.

For each regulatory input a, the recovery threshold $m_{\mathrm{th}}^{\mathrm{rec}}(a)$ was set according to the corresponding high-mark fixed point $m_{\mathrm{H}}(a)$. Let $\tau = 0$ denote the time at which the reactions were restored. The recovery time of a trajectory was defined as

$$T_{\mathrm{rec}} = \inf\{\tau > 0 : \hat{m}(\tau) \geq m_{\mathrm{th}}^{\mathrm{rec}}(a)\}. \tag{S50}$$

A trajectory was classified as recovered if $T_{\mathrm{rec}} \leq 10$. The recovery probability was calculated as

$$P_{\mathrm{rec}}(f_{\mathrm{del}}, a) = \frac{N_{\mathrm{rec}}}{N_{\mathrm{traj}}}, \tag{S51}$$

where N_{rec} is the number of recovered trajectories.

The recovery counts obtained at different f_{del} were fitted to a decreasing logistic function,

$$P_{\mathrm{rec}}^{\mathrm{fit}}(f_{\mathrm{del}}) = \frac{1}{1 + \exp\left[\kappa\left(f_{\mathrm{del}} - f_{\mathrm{del}}^{50}\right)\right]}, \tag{S52}$$

where κ controls the steepness. The fitted midpoint satisfies

$$P_{\mathrm{rec}}^{\mathrm{fit}}(f_{\mathrm{del}}^{50}) = 0.5. \tag{S53}$$

The fitted f_{del}^{50} was then compared with the mean-field prediction $1 - m_U/m_H$.

V. ACTIVATION–MAINTENANCE SIMULATIONS

The activation–maintenance simulations consisted of two consecutive stages. During activation, the system was evolved for $\tau = 10$ at the prescribed high trans-factor density ρ_W^{act}. The active density was then reduced to the fixed maintenance value

$$10^3 \rho_W^{\mathrm{maint}} = 2.96, \tag{S54}$$

and the simulation was continued for another $\tau = 10$.

The density reduction was implemented by converting randomly selected W particles into an inactive particle type I. The I particles interacted with all particle types through the background interaction strength $0.2\,k_{\mathrm{B}}T$, were excluded from the calculation of q_W, and had no writing activity. The remaining active factors corresponded to ρ_W^{maint}, while the total number of mobile particles remained unchanged. All other simulation parameters were unchanged during the switch.

VI. DYNAMICS UNDER PERIODIC STIMULATION

A. Triangular-wave stimulation

The active trans-factor density $\rho_W(\tau)$ was varied periodically while χ_Ω was held fixed. Because $a \propto \rho_W$, the regulatory input $a(\tau)$ followed the same triangular waveform. The stimulus frequency was denoted by ν, corresponding to a period $T = 1/\nu$. Within each cycle, let

$$h = \tau - nT, \qquad 0 \le h < T, \tag{S55}$$

denote the time elapsed since the beginning of that cycle, where $n = 0, 1, 2, \ldots$ is the cycle index. The input was then defined as

$$a(\tau) = \begin{cases} a_{\min} + 2(a_{\max} - a_{\min})\dfrac{h}{T}, & 0 \le h < T/2, \\ a_{\min} + 2(a_{\max} - a_{\min})\left(1 - \dfrac{h}{T}\right), & T/2 \le h < T. \end{cases} \tag{S56}$$

Thus, $a(\tau)$ increased linearly from $a_{\min}$ to $a_{\max}$ during the first half of each cycle and decreased linearly back to $a_{\min}$ during the second half. We used $a_{\min} = 0$ and $a_{\max} = 0.295$.

The active factor density $\rho_W(\tau)$ was varied by reversibly converting particles between the active type W and the inactive type I. At each update, particles were selected at random to match the prescribed triangular waveform. Only W particles contributed to q_W and possessed writing activity. The I particles interacted with all particle types through the background interaction strength $0.2\,k_{\mathrm{B}}T$. The total number of mobile particles remained unchanged. Simulations were initialized from $\hat{m}(0) = 0$. Fifty independent trajectories were simulated for each frequency, with each trajectory followed for up to four stimulation cycles.

B. Time-dependent prediction and hysteresis area

For the time-dependent input, the birth rate becomes

$$\lambda_n(\tau) = (N_\Omega - n)a(\tau)\mathcal{G}\left(\frac{n}{N_\Omega}\right), \tag{S57}$$

while the death rate remains $\mu_n = n$. The master equation was propagated numerically from $p_n(0) = \delta_{n0}$. The predicted ensemble-averaged mark fraction is

$$m(\tau) = \langle \hat{m}(\tau) \rangle = \sum_{n=0}^{N_\Omega} \frac{n}{N_\Omega} p_n(\tau). \tag{S58}$$

For the microscopic simulations, the hysteresis area was calculated separately for each of the 50 independent samples. For sample k, the hysteresis area of cycle j was calculated from its mark trajectory $\hat{m}^{(k)}(\tau)$. For discretely sampled

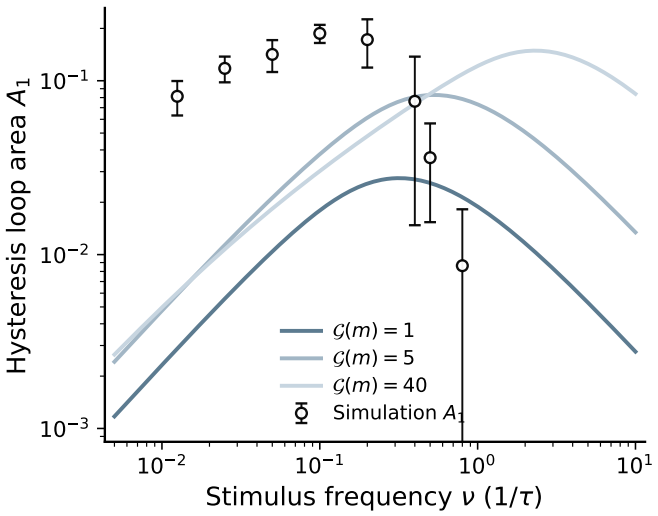

FIG. S9. First-cycle hysteresis area A_1 as a function of the stimulus frequency ν. Solid curves show birth–death predictions obtained by replacing the measured state-dependent enrichment with the constants $\mathcal{G} = 1$, 5, and 40. Open circles show the simulation results, and error bars denote standard deviations across trajectories. All cases use a triangular input with $a_{\min} = 0$ and $a_{\max} = 0.295$ and are initialized from $\hat{m}(0) = 0$.

points within cycle C_j,

$$A_j^{(k)} = \left| \sum_{\ell \in C_j} \frac{\hat{m}_{\ell+1}^{(k)} + \hat{m}_{\ell}^{(k)}}{2} \left(a_{\ell+1} - a_{\ell}\right) \right|. \tag{S59}$$

The mean hysteresis area was then obtained by averaging over independent samples,

$$\overline{A}_j = \frac{1}{N_{\text{traj}}} \sum_{k=1}^{N_{\text{traj}}} A_j^{(k)}, \tag{S60}$$

The corresponding standard deviation across trajectories was used as the error bar. The theoretical hysteresis areas were calculated from $\langle \hat{m}(\tau) \rangle$ using the same discrete integral procedure.

For the state-independent controls, the measured $\mathcal{G}(m)$ in Eq. (S57) was replaced by the constants $\mathcal{G} = 1$, 5, and 40 (Fig. S9). Constant enrichment produces a nonmonotonic frequency response, but no single constant reproduces the simulated response over the full frequency range.

C. Activation-cycle analysis

The response over the $(a_{\max}, \nu)$ parameter space was calculated from the time-dependent birth–death equation at fixed $a_{\min} = 0$. Each condition was initialized from $p_n(0) = \delta_{n0}$ and followed for a maximum of 20 cycles. The activation threshold was set to $m_{\text{act}} = 0.5$.

The activation cycle was defined as

$$n_{\text{act}} = \min\{j : \max_{\tau \in C_j} m(\tau) \geq m_{\text{act}}\}. \tag{S61}$$

Activation during the first cycle was classified as a direct response. Activation during cycles 2–20 was classified as temporal integration. Conditions that did not reach m_{act} within 20 cycles were classified as nonresponsive.

[1] A. Valouev, S. M. Johnson, S. D. Boyd, C. L. Smith, A. Z. Fire, and A. Sidow, Determinants of nucleosome organization in primary human cells, Nature **474**, 516 (2011).

[2] S. C. Parker, M. L. Stitzel, D. L. Taylor, J. M. Orozco, M. R. Erdos, J. A. Akiyama, K. L. Van Bueren, P. S. Chines, N. Narisu, N. C. S. Program, *et al.*, Chromatin stretch enhancer states drive cell-specific gene regulation and harbor human disease risk variants, Proc. Natl. Acad. Sci. **110**, 17921 (2013).

[3] W. A. Whyte, D. A. Orlando, D. Hnisz, B. J. Abraham, C. Y. Lin, M. H. Kagey, P. B. Rahl, T. I. Lee, and R. A. Young, Master transcription factors and mediator establish super-enhancers at key cell identity genes, Cell **153**, 307 (2013).

[4] S. Kadam, K. Kumari, V. Manivannan, S. Dutta, M. K. Mitra, and R. Padinhateeri, Predicting scale-dependent chromatin polymer properties from systematic coarse-graining, Nat. Commun. **14**, 4108 (2023).

[5] A. M. Chiariello, A. Abraham, S. Bianco, A. Esposito, A. Fontana, F. Vercellone, M. Conte, and M. Nicodemi, Multiscale modelling of chromatin 4d organization in sars-cov-2 infected cells, Nat. Commun. **15**, 4014 (2024).

[6] Z. Ibrahim, T. Wang, O. Destaing, N. Salvi, N. Hoghoughi, C. Chabert, A. Rusu, J. Gao, L. Feletto, N. Reynoird, *et al.*, Structural insights into p300 regulation and acetylation-dependent genome organisation, Nat. Commun. **13**, 7759 (2022).

[7] A. Serra-Cardona, S. Duan, C. Yu, and Z. Zhang, H3K4me3 recognition by the COMPASS complex facilitates the restoration of this histone mark following DNA replication, Sci. Adv. **8**, eabm6246 (2022).

[8] M. Kikuchi, S. Morita, M. Wakamori, S. Sato, T. Uchikubo-Kamo, T. Suzuki, N. Dohmae, M. Shirouzu, and T. Umehara, Epigenetic mechanisms to propagate histone acetylation by p300/CBP, Nat. Commun. **14**, 4103 (2023).

[9] A. R. Strom, J. M. Eeftens, Y. Polyachenko, C. J. Weaver, H.-F. Watanabe, D. Bracha, N. D. Orlovsky, C. C. Jumper, W. M. Jacobs, and C. P. Brangwynne, Interplay of condensation and chromatin binding underlies BRD4 targeting, Mol. Biol. Cell **35**, ar88 (2024).

[10] Y. Polyachenko, H.-F. Watanabe, A. Korolev, and W. M. Jacobs, Co-condensation and multivalency enable acetylation-sensitive, concentration-robust assembly of brd4 condensates (2026), arXiv:2606.02275 [physics.bio-ph].

[11] B. R. Sabari, A. Dall'Agnese, A. Boija, I. A. Klein, E. L. Coffey, K. Shrinivas, B. J. Abraham, N. M. Hannett, A. V. Zamudio, J. C. Manteiga, C. H. Li, Y. E. Guo, D. S. Day, J. Schuijers, E. Vasile, S. Malik, D. Hnisz, T. I. Lee, I. I. Cisse, R. G. Roeder, P. A. Sharp, A. K. Chakraborty, and R. A. Young, Coactivator condensation at super-enhancers links phase separation and gene control, Science **361**, eaar3958 (2018).

[12] Y. Zhang, K. Brown, Y. Yu, Z. Ibrahim, M. Zandian, H. Xuan, S. Ingersoll, T. Lee, C. C. Ebmeier, J. Liu, D. Panne, X. Shi, X. Ren, and T. G. Kutateladze, Nuclear condensates of p300 formed though the structured catalytic core can act as a storage pool of p300 with reduced HAT activity, Nat. Commun. **12**, 4618 (2021).

[13] M. Kosno, S. L. Currie, A. Kumar, C. Xing, and M. K. Rosen, Molecular features driving condensate formation and gene expression by the BRD4-NUT fusion oncoprotein are overlapping but distinct, Sci. Rep. **13**, 11907 (2023).

[14] B. M. Zee, R. S. Levin, P. A. DiMaggio, and B. A. Garcia, Global turnover of histone post-translational modifications and variants in human cells, Epigenet. Chromatin **3**, 22 (2010).

[15] Y. Zheng, P. M. Thomas, and N. L. Kelleher, Measurement of acetylation turnover at distinct lysines in human histones identifies long-lived acetylation sites, Nat. Commun. **4**, 2203 (2013).

[16] D. T. Gillespie, Exact stochastic simulation of coupled chemical reactions, J. Phys. Chem. **81**, 2340 (1977).

[17] S. Heinz, C. E. Romanoski, C. Benner, and C. K. Glass, The selection and function of cell type-specific enhancers, Nat. Rev. Mol. Cell Biol. **16**, 144 (2015).

[18] J. A. Anderson, J. Glaser, and S. C. Glotzer, Hoomd-blue: A python package for high-performance molecular dynamics and hard particle monte carlo simulations, Comput. Mater. Sci. **173**, 109363 (2020).

[19] P. J. Huber, Robust estimation of a location parameter, in *Breakthroughs in statistics: Methodology and distribution* (Springer, 1992) pp. 492–518.

[20] S. Karlin, *A first course in stochastic processes* (Academic press, 2014).

[21] A. S. Novozhilov, G. P. Karev, and E. V. Koonin, Biological applications of the theory of birth-and-death processes, Briefings Bioinf. **7**, 70 (2006).

[22] M. A. Micheelsen, N. Mitarai, K. Sneppen, and I. B. Dodd, Theory for the stability and regulation of epigenetic landscapes, Phys. Biol. **7**, 026010 (2010).